

Spitzer Observations of Optically “Invisible” Radio And X-Ray Sources: High Redshift AGN

J. L. Higdon¹, S. J. U. Higdon¹, D. W. Weedman¹, J. R. Houck¹, E. Le Floch^{h2}, M. J. I. Brown³, A. Dey⁴, B. T. Jannuzi⁴, B. T. Soifer⁵, & M. J. Rieke²

ABSTRACT

We have combined a survey at $24\ \mu\text{m}$ to 0.3 mJy with the Multiband Imaging Photometer (MIPS) on the Spitzer Space Telescope, a 20 cm A-array Very Large Array survey covering $0.5\ \text{deg}^2$, and an existing 172 ks Chandra X-Ray Observatory exposure to investigate the nature of optically faint radio and X-ray sources in the NOAO Deep Wide-Field Survey (NDWFS) in Boötes. We find little overlap between the radio and infrared selected populations: only 9% of the infrared sources are detected in the radio and only 33% of the radio sources are detected in the infrared. Thirty-six (10%) of the 377 compact radio sources lack optical counterparts in the NDWFS B_W , R , & I images. We refer to these objects as optically invisible radio sources (OIRS). Only four (13%) of the thirty-one OIRSs observed with MIPS are detected at $24\ \mu\text{m}$. Comparisons of the radio and infrared properties of the OIRSs with various galaxy spectral energy distributions demonstrate that most of these sources are powered by AGN rather than starbursts. Similarly, eleven X-ray sources observed by both MIPS and the VLA are classified as optically invisible X-ray sources (OIXS). None are detected at $24\ \mu\text{m}$ or 20 cm. All seven OIXSs detected in Chandra’s 0.5-2 keV band have infrared to X-ray flux ratios consistent with their luminosity being dominated by an unobscured AGN. From these results we conclude that both the optically invisible radio and X-ray source populations are primarily AGN, relatively unaffected by dust and most likely at $z > 1$. No OIRSs are detected in X-ray emission and no OIXSs are detected at 20 cm. However, given the wide range in radio and X-ray properties of known AGN and the size of our samples, this lack of overlap does not necessarily imply different AGN source populations.

¹Astronomy Department, Cornell University, Ithaca, NY 14853

²Steward Observatory, University of Arizona, Tucson, AZ 85721

³Astronomy Department, Princeton University, Princeton, NJ 85726

⁴National Optical Astronomy Observatory, Tucson, AZ 85726

Subject headings: galaxies: high-redshift – galaxies: starburst – galaxies: AGN
– infrared: galaxies – radio: galaxies – X-ray: galaxies

1. Introduction

Determining the star formation density of the Universe beyond $z \sim 1$ and the contribution made by AGN to the luminosity evolution of galaxies are two fundamental goals of observational cosmology. Addressing these questions requires observations at wavelengths capable of locating intrinsically luminous sources that are either heavily obscured by dust, or so distant that their rest-frame optical wavebands fall below the cutoff for intergalactic hydrogen absorption (i.e., the Lyman limit). Locating and understanding such obscured sources is a fundamental objective of the *Spitzer Space Telescope* (Spitzer; Werner et al. 2004) mission¹, which is capable of identifying $z > 1$ galaxy populations that are luminous at infrared wavelengths but faint optically due to the effects of dust. Starbursts and AGN are expected to be powerful emitters at radio wavelengths due to large populations of radio-luminous supernova remnants for starbursts and accretion disk phenomena for AGN. Indeed, sensitive radio surveys routinely find populations of sub-mJy point sources with either very faint optical counterparts or no counterparts at all (e.g., Richards et al. 1999; Fomalont et al. 2002). Whether these sources represent dust enshrouded starburst galaxies at $z \sim 1-3$ or radio loud AGN at $z > 4$ has yet to be determined conclusively. This suggests as a strategy for locating heavily obscured starbursts and AGN at high redshifts the definition of infrared and radio source populations that are either extremely faint at all optical bands or “invisible”, i.e., objects that can not be distinguished from the background in deep optical images.

The NOAO Deep Wide-Field Survey² (NDWFS; Jannuzi & Dey 1999) provides multi-band optical imagery to very faint magnitudes over large survey areas, and so is uniquely suited for comparison to other surveys in search of sources that are optically invisible. In particular, the NDWFS field in Boötes covers ~ 9.3 deg² to sensitivities in B_W , R , & I of ap-

¹The Spitzer Space Telescope is operated by JPL, California Institute of Technology for the National Aeronautics and Space Administration. Information on Spitzer can be found at <http://ssc.spitzer.caltech.edu/>

²The NOAO Deep Wide-Field Survey is supported by the National Optical Astronomy Observatory, which is operated by AURA, Inc., under a cooperative agreement with the National Science Foundation. Information on the NDWFS can be found at <http://www.noao.edu/noao/noaodeep/>.

proximately 26.5, 25.5, & 24.7 (Vega) magnitudes respectively.³ To explore the mid-infrared characteristics of this data set, we have surveyed most of the Boötes field at wavelengths of 24, 70, & 160 μm with Spitzer’s Multiband Imaging Photometer (MIPS; Rieke et al. 2004). At 24 μm the point source sensitivity is 0.3 mJy (5σ) and the angular resolution is $5.5''$ (FWHM). We will present other results of this infrared survey in more detail in future publications, although the survey and analysis techniques have been described by Papovich et al. (2004).

Deep and high resolution radio data are important for a full understanding of the nature of the sources detected by MIPS. This follows from the well established tight correlation between infrared and radio flux densities in star forming galaxies (de Jong et al. 1985; Helou et al. 1985), which is a consequence of the life (re-radiation of UV photons by dust) and death (SNe remnants) of massive stars. As a result, the ratio of infrared to radio flux densities provides a means of distinguishing starbursts from AGN. Moreover, the sub-arcsecond positional accuracy attainable with radio interferometric surveys allows confident matching of sources discovered in infrared surveys, which can have poorer spatial resolution. This is especially important if a source is indeed optically invisible. For these reasons, we conducted sensitive and high angular resolution observations of a 0.5 deg^2 subregion within the Boötes field with the *Very Large Array* (VLA) at 20 cm. These observations were designed to detect dusty starburst galaxies with 24 μm flux densities greater than 0.75 mJy based on their expected spectral energy distributions and likely redshift range.⁴ Although the MIPS 24 μm survey reaches a fainter limit than this, we chose this infrared limit for matching radio observations because we were primarily interested in selecting sources bright enough to obtain spectra with the Infrared Spectrograph (IRS; Houck et al. 2004) on Spitzer (i.e., Higdon et al. 2004, Houck et al. 2005).

Our survey region was chosen to overlap the northern Large Area Lyman Alpha survey field (LALA; Rhoads et al. 2000), which includes an extremely deep (172 ks) *Chandra X-Ray Observatory* integration by Wang et al. (2004), centered at RA = $14^h 25^m 37.79^s$ and Dec = $+35^\circ 36' 00.2''$ and covering 0.1 deg^2 . The X-ray point source sensitivities are $1.5 \times 10^{-16}\text{ erg s}^{-1}\text{ cm}^{-2}$ in the “soft” 0.5-2.0 keV band and $1.0 \times 10^{-15}\text{ erg s}^{-1}\text{ cm}^{-2}$ in the “hard” 2.0-7.0 keV band (both 5σ). Only the North and South Chandra Deep Fields (2 and 1 Ms integrations respectively) are substantially deeper. As a result, there was minimal overlap with the much more extensive 20 cm survey of the Boötes field by de Vries et al. (2002) using

³These represent the 50% completeness limits in the source catalogs for the area involved in this study. Similar sensitivities are expected throughout the survey.

⁴For these estimates we used the starburst infrared/radio correlation of Yun et al. (2001) together with K-corrections from the SED templates of Lagache et al. (2002).

the Westerbork Synthesis Radio Telescope (WSRT). In this paper we will use the combined X-ray, optical, infrared, and radio catalogs to investigate the nature of *Optically Invisible Radio and X-ray Sources* (OIRS & OIXS) in our radio survey area. These are defined to be X-ray and compact radio sources that have no apparent counterparts in the NDWFS B_W , R , & I images. In addition, we wish to see how the properties of these two optically invisible populations compare with one another.

The outline of this paper is as follows: we first discuss the VLA observations and data reduction in §2. This is followed by a brief discussion of the radio source catalog in §3 and our criteria for matching sources from the MIPS, Chandra, and VLA surveys. We then describe the infrared, radio, and X-ray properties of the optically invisible radio and X-ray sources (§4) in order to constrain the dominant source of their luminosity. Finally, before summarizing in §6, we compare the average space densities of the OIRSs and OIXSs with those of other galaxies, including quasars, and also consider whether OIRSs and OIXSs are drawn from the same population in §5. Throughout this paper, we have assumed a flat Λ CDM cosmology with $\Omega_M=0.27$, $\Omega_\Lambda=0.73$, and a Hubble constant of $71 \text{ km s}^{-1} \text{ Mpc}^{-1}$.

2. Radio Observations And Reduction

We observed three overlapping fields within the NDWFS in Boötes with the VLA in the A-configuration at 20 cm. These fields, labeled North, East, and South, are shown in Figure 1, which also depicts the Chandra survey field of Wang et al. (2004). The field center coordinates and other details of the observational setup are given in Table 1. Spectral line mode was used to minimize bandwidth smearing and facilitate the flagging of narrow band radio interference. The correlator was configured to provide two sets of seven channels (3.125 MHz separation), each centered at 1.3649 and 1.4351 GHz. Both left and right handed circular polarizations were measured at the two frequencies. Each field was observed in 40 minute blocks, inter-spaced with 2 minute observations of the nearby secondary calibrator 1416+347 ($S_{1.435 \text{ GHz}} = 1.96 \pm 0.01 \text{ Jy}$) to correct drifts in the antenna gains and phases. Flux and bandpass calibration were accomplished with longer observations of the primary flux calibrator 3C 48 ($S_{1.435 \text{ GHz}} = 15.01 \pm 0.01 \text{ Jy}$, Baars et al. 1977) made at the start of each night. On-source integrations totaling 5.5, 4.9, and 5.4 hours were achieved at the North, East, and South positions, respectively.

The visibilities were processed using routines in NRAO’s Astronomical Imaging Processing System (AIPS) software package. A standard antenna based calibration was applied to each data set after excising a very small fraction of the data that was corrupted by radio interference. The routine IMAGR was used to map the primary beam with the correct

w-phase terms (DO3DIMAG=1). Images were made using a robust weighting parameter of 1.1, which improved the beam shape at the expense of an $\sim 7\%$ increase in noise. Radio sources from the FIRST catalog (Becker et al. 1995) that were located outside the primary beams yet capable of contributing significant side lobes were also cleaned. Self-calibration was helpful in improving the antenna based calibration, particularly in the South field, which is dominated by a double-lobed radio source (87GB 142337.6+351136). After convolving to a common resolution of $1.40''$ FWHM, the three final images were placed on a common grid and combined. The resulting rms at the three field centers is $\sim 15 \mu\text{Jy beam}^{-1}$, which is in good agreement with the expected noise levels using the array parameters listed in the VLA Observational Status Summary. Since we have imaged only three array pointings, significant variations in sensitivity exist across the survey field. Close to the field centers where the sensitivity is the highest we can detect point sources as faint as $\sim 80 \mu\text{Jy}$. However, the faintest point source we are capable of detecting throughout the entire survey is $\sim 200 \mu\text{Jy}$. For this reason we do not attempt to produce a radio source catalog that is complete to a given flux density limit. This does not affect our ability to calculate flux density ratios and limits for the radio, infrared, and X-ray sources. However it will impact our estimates of surface densities.

3. Source Identification And Matching

We restricted our radio survey to where the sensitivity in the combined pointings exceeded 40% of the pointing centers, i.e., where the 1σ noise is less than $37 \mu\text{Jy beam}^{-1}$. This corresponds to a total area of 0.5 deg^2 . We used SExtractor (Bertin & Arnouts 1996) to identify radio sources in our survey rather than the AIPS routine SAD or its variants, even though SExtractor is more commonly used to find and catalog sources in optical images. This was because of the package’s flexibility and our experience using it. After first smoothing the input radio image with a Gaussian profile matching the synthesized beam, SExtractor identified groups of at least five contiguous pixels, each exceeding the locally defined 2.5σ background fluctuations. From this first cut of source identification, only those with a peak pixel value exceeding five times the local background rms were classified as source candidates. These were checked visually, and the small fraction found to be detections of residual sidelobes or radio source structure (e.g., hot spots in jets) were deleted from the catalog. A total of 392 sources satisfied these selection criteria, of which 377 are point-like or marginally resolved. These objects are classified as “compact” objects in the radio source catalog. Flux densities were measured using the AIPS task IMFIT with the final primary beam corrected image. We determined fluxes for extended objects using the AIPS task BLSUM.

We estimated the number of false detections in our survey by running SExtractor with the same settings on the radio image multiplied by -1. Assuming that the background noise is symmetric with respect to the mean, the number of sources detected in the reversed image should equal the number of false positives. Only three negative “sources” were found that were not associated with side-lobes, and all of these were < 5.5 times the local rms. As a check of this analysis, we calculated the number of independent beams in the radio survey and then estimated the number of $\geq 5 \sigma$ detections one would expect from random fluctuations. For 5×10^6 beams we expect only two spurious 5σ detections and none at the 6σ level. We therefore expect minimal contamination of our radio catalog by false sources, with two to three of the nearly four-hundred detections being spurious.

We compared the coordinates of the compact sources with the NDWFS optical catalog.⁵ It was found that two-thirds of the radio sources had an optical counterpart within $0.3''$. Because the great majority of these identifications are real, this value was taken as the 1σ relative positional accuracy. Similarly, the measured 1σ scatter in ΔRA and ΔDec between the $24 \mu\text{m}$ sources and their nearest optical counterparts is $0.3''$ for $F_{24\mu\text{m}} \geq 0.75$ mJy. The positional accuracy was somewhat worse ($\sim 1''$) for the MIPS sources near 0.3 mJy. The positional accuracy of the “soft” band X-ray sources listed in Table 1 of Wang et al. (2004) ranges from 0.3 to $3.5''$, but is typically $1''$. We will adopt this as the X-ray source positional accuracy.

The identification of optically invisible radio sources was a two step process. First we correlated the positions of all 377 compact radio sources with the NDWFS B_W , R , and I -band catalogs, stipulating that OIRS candidates must not have a cataloged optical counterpart centered within a $1.5''$ radius (5σ). For the candidates passing this test, we inspected the NDWFS images at these positions to verify that no optical source was visible in any band. A small number of candidates without apparent optical counterparts but close to the edges of field galaxies were also rejected. This process yielded thirty-six OIRSs, which we list in Table 2. The identification of optically invisible X-ray sources was carried out in a similar manner, starting with the thirteen sources in Table 1 of Wang et al. (2004) with positional uncertainties less than $2''$ that lack B_W , R , & I counterparts.

To determine if the OIRSs and OIXSs had infrared counterparts, we then compared their positions with the MIPS $24 \mu\text{m}$ catalog ($F_{24\mu\text{m}} \geq 0.3$ mJy), calling a radio and infrared source matched if their positions differed by less than $2.5''$. Infrared fluxes or upper-limits for the OIRSs are given in Table 2. Similarly, we adopted as criteria for matching radio to

⁵Catalogs were derived using the third data release (DR3) version of the NDWFS optical images (Jannuzi et al. in preparation, <http://www.noao.edu/noao/noao-deep>).

X-ray and X-ray to infrared sources that their coordinates agree to $< 2''$.

4. Results And Analysis

4.1. Properties Of The OIRS Population

We identified a total of thirty-six OIRSs over the 0.5 deg^2 survey area, a number representing 10% of the total compact radio source population. Table 2 lists their radio catalog number, source name incorporating J2000 coordinates, and physical properties. Nearly all (86%) are detected above the 5.5σ level, where we expect no spurious sources. Figure 2 shows $12'' \times 12''$ sub-images from the NDWFS B_W , R , and I data centered on five of the OIRSs, along with the corresponding sub-images from the MIPS $24 \mu\text{m}$ survey field. The radio continuum source structure for each is shown contoured on the I-band sub-images, with the lowest contour representing the local 3σ noise level in the radio image.

The precise magnitude limit for an OIRS will depend on the position of the source in the NDWFS field. We therefore derived B_W , R , and I upper-limits for the 31 OIRS within $2''$ diameter apertures centered on their positions using the appropriate NDWFS zero-point constants.⁶ Typical magnitude limits are 27.0, 25.7, and 25.0 (Vega) in B_W , R , and I , respectively. These are listed in Table 2 for each source. Figure 3 shows a histogram of the integrated 20 cm continuum flux densities for the OIRS sample. Nearly 90% are sub-mJy radio sources (median $F_{20\text{cm}}^{\text{total}} = 0.40 \text{ mJy}$), though five have flux densities greater than 1 mJy. Source #362 possesses the peak flux density for the sample of nearly 7 mJy. Thirty-one OIRSs were included within the MIPS survey area. Only four of these - sources # 97, 176, 245, and 363 in Table 2 - were detected at $24 \mu\text{m}$ above 5σ . We stack-averaged the remaining twenty-seven MIPS sub-images in an attempt to detect fainter emission levels. No significant signal was detected, and we set an upper-limit on the average infrared flux density for the ensemble of $F_{24\mu\text{m}} < 60 \mu\text{Jy}$ (5σ).

The small number of radio/infrared matches (13%) is a significant result, since from the surface densities of the 20 cm and $24 \mu\text{m}$ sources, we estimate the probability of a random match to be less than 1%. We verified the lack of overlap between these two source populations by plotting the OIRSs' positions on the MIPS $24 \mu\text{m}$ image and inspecting the result visually. Two of these MIPS detected sources are shown in the bottom two rows of Figure 2. Eight OIRSs are situated in the survey area covered by both Chandra and MIPS

⁶Limits were calculated using $q_0 - 2.5 \log(5 \times \text{rms} \times \sqrt{N_{\text{pix}}})$, where N_{pix} and rms are the number of pixels and variance within the $2''$ diameter aperture respectively, and q_0 is the zero-point constant.

(0.08 deg²). None were detected at 24 μm or in any of the X-ray bands. This sets upper-limits of 0.3 mJy at 24 μm and 1.5×10^{-16} erg s⁻¹ cm⁻² in the 0.5-2.0 keV X-ray band for this sub-sample.

Because of the variable sensitivity throughout the radio images, simply dividing the number of OIRSs by the survey area would lead to an under-estimate of their true surface density (σ_{OIRS}). This is due to the fact that the fainter radio sources can only be detected near the pointing centers where the sensitivity is the highest. We have attempted a first-order correction to this effect by first weighting each OIRS by the ratio of the total survey area to the area where it could have been detected given its peak 20 cm flux density (Hopkins et al. 1999). Doing so resulted in an average surface density of $\sigma_{\text{OIRS}} = 104 \pm 17$ deg⁻², where the uncertainty represents Poisson counting errors only. There is a strong dependence on flux density. We divided the OIRSs into three flux density bins, $F_{20\text{cm}}^{\text{peak}} < 400$ (17 sources), 400-600 (13 sources), and > 600 (6 sources) $\mu\text{Jy beam}^{-1}$, and calculated the average surface density for each as above. We find that $\sigma_{\text{OIRS}}(< 400 \mu\text{Jy beam}^{-1}) = 66 \pm 12$ deg⁻², $\sigma_{\text{OIRS}}(400-600 \mu\text{Jy beam}^{-1}) = 26 \pm 11$ deg⁻², and $\sigma_{\text{OIRS}}(> 600 \mu\text{Jy beam}^{-1}) = 12 \pm 5$ deg⁻², i.e., the OIRS surface density increases with decreasing 20 cm flux density.

4.2. Are The OIRSs Powered By Star Formation Or AGN?

The logarithm of the infrared to radio continuum flux density ratio, or q , is a useful parameter for distinguishing sources powered by massive star formation from AGN, and especially radio-loud AGN. In Figure 4 we show the distribution of q using the MIPS 24 μm and 20 cm radio continuum data in Table 2 for the OIRS sample (i.e., $q = \log(F_{24\mu\text{m}}/F_{20\text{cm}})$). The four OIRSs detected by MIPS are represented by the shaded histogram bins ($-0.5 \leq q \leq 0.5$). For the twenty-seven other OIRSs we show a histogram of upper-limits for q , using $F_{24\mu\text{m}} = 0.3$ mJy in the calculation. The small number of sources precludes a strong conclusion statistically, but we note that three of the four OIRSs with MIPS detections have positive values of q , with a mean of 0.29. Only source #97 has a negative q . On the other hand, of the 27 OIRSs not detected by MIPS, two-thirds (18 of 27) have negative q values. Since these are all upper-limits, it is likely that even a larger fraction of these sources will have $q < 0$.

We first considered the origin of the OIRSs' emission by comparing the values and upper-limits of q in Table 2 to those derived from local starbursts and AGN for a range of redshifts. Using the most luminous galaxy ($3 \times 10^{12} L_{\odot}$) SED from Lagache et al. (2002), we calculated the observer's frame $F_{850\mu\text{m}}/F_{24\mu\text{m}}$ ratio for redshifts of 1, 2, and 3. This in turn was used with the scaling in Chary & Elbaz (2001) to calculate the corresponding 20 cm flux

densities. Under these assumptions, starburst galaxies with 20 cm flux densities of 200 μJy should have 24 μm flux density of 2.8 mJy at $z = 1$, 2.4 mJy at $z = 2$, and 1.6 mJy at $z = 3$. In short, starbursts detected in our radio survey would be easily detected in our 24 μm data. These will in turn give rise to values of q equal to 1.15, 1.08, and 0.90 for starbursts at these three redshifts. This is in agreement with Appleton et al. (2004), who found that for flux densities measured at 24 μm and 20 cm, starburst dominated systems have $q = 0.8 \pm 0.3$ for $z \lesssim 2$. This range is represented in Figure 4 as the solid and dashed vertical lines. The values of q for starburst dominated systems are substantially greater than the upper-limits shown, and even appear significantly larger than the q 's determined for the four OIRSs detected by MIPS. Thus for virtually the entire OIRS sample a clear enhancement in radio continuum emission over that expected for a pure starburst is evident. This indicates the presence of a dominant AGN component.

A more detailed illustration with a broader range of SED type is presented in Figure 5, where q is plotted against the logarithm of 20 cm flux density. Four families of curves are shown, representing (from top to bottom) (1) a normal Sc galaxy with a SFR of $3 M_{\odot} \text{ yr}^{-1}$, (2) a high luminosity starburst/ULIRG with a $3000 M_{\odot} \text{ yr}^{-1}$ SFR, (3) a type 2 Seyfert AGN (NGC 262), and (4) a QSO with 3C 273's spectral energy distribution. The late spiral, ULIRG, and AGN/Seyfert SEDs were taken from the compilation of Xu et al. (2001), while the 3C 273 SED was taken from the NED online database. For the two star forming galaxy templates, we first calculated the rest-frame 20 cm luminosity ($L_{20\text{cm}}$ in W Hz^{-1}) for a given star formation rate (in $M_{\odot} \text{ yr}^{-1}$) using the calibration given in Equation 6 of Bell (2003). Using this value and the SED we derived the observer-frame $F_{24\mu\text{m}}/F_{20\text{cm}}$ ratio as a function of redshift from $z = 0.1$ -7.0. We next calculated the observer-frame 20 cm flux density ($F_{20\text{cm}}$, in μJy) for these redshifts using

$$L_{20\text{cm}} = 1.26 \times 10^{-35} F_{20\text{cm}}^2 d_L^2 (1+z)^{\alpha-1} \quad (\text{W Hz}^{-1}), \quad (1)$$

where d_L is the luminosity distance in cm. The radio spectral index α (where $F_{\lambda} \propto \lambda^{\alpha}$) was derived from the SED templates over the wavelength range 7 to 20 cm. The starburst, normal, and AGN templates gave similar average spectral indices (mean $\alpha = 0.65$). For the two AGN we considered 20 cm luminosities of 10^{25} and $10^{26} \text{ W Hz}^{-1}$, and calculated observer-frame $F_{24\mu\text{m}}/F_{20\text{cm}}$ ratios and 20 cm flux densities as above, also for the redshift range $z = 0.1$ -7.0. The resulting four sets of tracks are indexed by redshift from $z = 0.1$ to 7.

The four MIPS detected OIRSs are shown as unfilled squares in Figure 5. For three (#176, 245, & 363), their positions are consistent with the $\text{SFR} = 3000 M_{\odot} \text{ yr}^{-1}$ ULIRG template over a $z=2$ -3 redshift range, albeit somewhat displaced below the track. Note that increasing/decreasing the SFR for either the ULIRG or Sc galaxy templates has the

effect of moving the tracks to the right/left. The vertical position is controlled solely by the shape of the SED and redshift. It is therefore possible that these could be at $z = 4-7$ if of sufficient luminosity. The other MIPS detected OIRS (#97) is situated well below the ULIRG track, with $q = -0.24 \pm 0.21$. The remaining twenty-seven OIRSs with q upper-limits are shown as filled circles with arrows. Again, two-thirds of them have negative values of q , which is inconsistent with late spiral or ULIRG SEDs at any redshift. These sources show a clear excess in radio emission relative to the infrared compared to a system powered by star formation. The q upper-limits cannot be used to distinguish between Seyfert and quasar templates in Figure 5 (both require $q \lesssim -1$ for all z). However, it is clear that the bulk of the OIRSs are powered primarily by an AGN, with many being radio-loud.

4.3. Are The OIXSs Starbursts Or AGN Powered Systems?

X-ray sources with very faint optical counterparts, or no counterparts at all, are also found in deep surveys (e.g., Barger et al. 2003). Like the optically faint radio source population, these objects have been proposed to represent highly obscured starburst galaxies or AGN at very high redshift, or possibly even AGN which are over-luminous in X-rays compared to local examples. To investigate the nature of these sources, we examined the eleven X-ray sources in Table 1 of Wang et al. (2004) without B_W , R , & I counterparts that were observed by MIPS at $24 \mu\text{m}$. The properties of these OIXSs, including source number (taken from Table 1 in Wang et al. 2004), J2000 coordinates, “soft” band X-ray fluxes or upper-limits, and optical limits are given in Table 3. Also listed are the OIXSs’ X-ray “hardness ratio” (HR), defined as $\text{HR} = (\text{H}-\text{S})/(\text{H}+\text{S})$, where H and S represent the “hard” 2-7 keV and “soft” 0.5-2 keV band counts, respectively.

No OIXSs were detected at $24 \mu\text{m}$. This has important consequences for the origin of their X-ray luminosity. Weedman et al. (2004) used infrared and X-ray spectra from a sample of nine starburst regions in four merging systems and three obscured AGN to determine empirically that the ratio IR/X (defined to be the $24 \mu\text{m}$ flux density in mJy to the Chandra 0.5-2.0 keV flux in units of $10^{-16} \text{ erg s}^{-1} \text{ cm}^{-2}$) has a lower bound of 0.2 for starbursts and obscured AGN for $z \leq 3$. Ratios of IR/X smaller than 0.2 indicate that the source is powered by a relatively unobscured AGN. Note that we should detect any “soft” band X-ray source in Wang et al. (2004)’s survey that is powered by a starburst or heavily obscured AGN (i.e., $\text{IR}/\text{X} > 0.2$) given the Chandra and MIPS $24 \mu\text{m}$ sensitivities. This empirical criterion can be used to classify the seven OIXSs in our MIPS survey that were detected in the “soft” X-ray band. Figure 6 shows a plot of IR/X versus the X-ray hardness ratio for these sources. All seven have values of $\text{IR}/\text{X} < 0.2$, which clearly indicates the

presence of a dominant unobscured AGN. We can not classify the four OIXSs in Table 3 with “soft” band upper-limits. Nevertheless, at least 64% (7/11) of the OIXSs are powered by unobscured AGN.

The X-ray hardness ratio can be used to place rough constraints on the redshift distribution of the OIXSs. Wang et al. (2004) argued that the X-ray spectrum will soften with increasing redshift, with $HR < 0.6$ marking $z \gtrsim 1$ objects. In support of this, Wang et al. (2004) determined photometric redshifts for five X-ray sources detected at I and z' bands but not in R . The three with $z_{\text{phot}} \sim 1-2$ have hardness ratios between -0.1 and 0.6 , while the two “softest” sources ($HR \lesssim -0.5$) have $z_{\text{phot}} \sim 4.3$. By this criteria, nine out of the eleven OIXSs in our sample can have $z > 1$ ($HR < 0.6$). Four can possibly at $z \sim 4-5$ ($HR < -0.5$).

No OIXSs were detected by our radio survey, which sets a 20 cm flux density limit of $\sim 200 \mu\text{Jy}$ for these sources. Note that at these levels we would have easily detected radio loud quasars with 3C 273-like SEDs and 20 cm luminosities greater than $10^{25} \text{ W Hz}^{-1}$ beyond redshifts of six (Figure 5), and most Seyfert systems with similar 20 cm luminosities. OIXSs thus appear to be largely a population of radio-quiet AGN.

4.4. Comparison Of Radio, Infrared, & X-Ray Source Catalogs

This study is concerned primarily with the optically invisible source populations. However, it is worthwhile considering the characteristics of the radio, infrared, and X-ray populations as a whole. Because of the tight correlation between infrared and radio flux densities for infrared-luminous galaxies (de Jong et al. 1985; Helou et al. 1985) and because of the indications that the sub-mJy radio population corresponds to faint, star-forming galaxies (e.g., Haarsma et al. 2001), a strong overlap between the radio and MIPS survey samples might be expected. Such an overlap is implied by the results displayed from analogous work in the First Look Survey (FLS) area, for which Appleton et al. (2004) show a clear correlation between flux densities at $24 \mu\text{m}$ and at 20 cm (see their Figure 2). However, the sources plotted there are only those detected in both infrared and radio with redshifts less than ~ 2 , which does not provide a comparison of the entire radio and infrared samples in the FLS survey region.

Table 4 shows various source detection statistics for our radio, infrared, and X-ray survey regions. First, we note that our radio survey does not go sufficiently deep to detect the majority of MIPS sources. Within the 0.5 deg^2 VLA survey area there are 1405 MIPS detections, and 377 compact radio sources. Only 125 are detected in both wavebands. That

is, 9 ± 1 % of the infrared sources have radio counterparts and 33 ± 3 % of the radio sources have MIPS counterparts with fluxes of at least 0.3 mJy. This is not too surprising since our radio observations were intended to detect the $F_{24\mu\text{m}} \geq 0.75$ mJy source population. There are 216 such 24 μm sources in our survey area. Only 33 ± 5 % of these have radio counterparts. Similarly, 23 ± 3 % of the compact radio sources have infrared counterparts > 0.75 mJy at 24 μm . Sensitivity variations will of course introduce a bias against detecting faint radio sources far away from the three pointing centers. However, we do not see a large effect. If we restrict ourselves to regions where the radio rms is less than $17 \mu\text{Jy beam}^{-1}$, i.e., an area of 0.17 deg^2 , we find similar detection fractions: 32 ± 7 % (25/78) of the $F_{24\mu\text{m}} \geq 0.75$ mJy sources have radio counterparts, while 19 ± 4 % (25/130) of the compact radio sources MIPS counterparts with $F_{24\mu\text{m}} \geq 0.75$ mJy. This shows that greater 20 cm sensitivities are required to detect the bulk of the infrared sources for which IRS spectra can be obtained in reasonable integration times.

When comparing the radio and infrared populations, it is therefore important to realize that only a relatively small fraction of sources are detected in both bands. This is illustrated in Figure 7, where we show histograms of q for the 125 sources detected at both 24 μm and 20 cm (thick solid line), the 194 radio sources not detected at 24 μm (thin dashed line), and the 1086 24 μm sources with no measured radio fluxes (thick dashed line). For the radio-only sample we calculated q upper-limits using $F_{24\mu\text{m}} = 0.3$ mJy. For the infrared-only detected sample we calculated lower-limits for q by setting $F_{20\text{cm}}$ equal to that of a point source with a peak flux density $5\times$ the radio image rms at the infrared source’s position.

The sources detected at both 24 μm and 20 cm show a distribution of q that peaks at ~ 0.5 . This is in reasonable agreement with Appleton et al.’s (2004) result that $q = 0.8 \pm 0.3$ for the radio-infrared correlation at $z \lesssim 2$. The smaller range of q evident in Figure 7 may be partly due to the detection of $z > 2$ ULIRGS, which will have progressively smaller q with increasing redshift (see the ULIRG track in Figure 5). This is consistent with a population of galaxies powered primarily by star formation, though an AGN contribution is still possible. Radio-loud AGN are certainly apparent in the negative q tail. AGN also clearly dominate the population of radio sources with no MIPS detections in Figure 7. However, the bulk of the infrared sources in the radio survey field have only lower-limits for q , with a strong peak between 0.5 and 1. While this is consistent with star formation being the dominant power source, deeper 20 cm observations will be required to measure q and quantify the radio-infrared correlation for the majority of galaxies in the survey. Figure 7 suggests that the radio and infrared selected populations do not overlap, i.e., that each represents populations of AGN and starburst dominated galaxies, respectively. Higher sensitivity radio and infrared observations will be needed to verify this.

An important related question is whether the OIRSs represent a population significantly different from the radio sources with optical counterparts, whose characteristics (e.g., starburst or AGN dominated) can be determined through optical or near-infrared spectroscopy. There is a qualitative indication that this might be so from the overall difference in the infrared detection rate for radio sources in the OIRS sample compared to the full radio sample. We find that $33 \pm 3\%$ of the compact radio sources in the entire sample are detected in the infrared to the 5σ sensitivity limit, whereas only $13 \pm 7\%$ of the OIRS are detected. Here the uncertainties represent Poisson statistics only. While this suggests a difference in the two radio populations, the small number of sources in the OIRS sample prevents this from being a statistically robust conclusion.

In the portion of the field covered by both Chandra and Spitzer surveys ($\sim 0.07 \text{ deg}^2$), there are 240 $24 \mu\text{m}$ sources brighter than 0.3 mJy (see Table 4), and 104 Chandra “soft” band sources brighter than $1.5 \times 10^{-16} \text{ erg s}^{-1} \text{ cm}^{-2}$. Only 18 sources are detected in both infrared and X-ray bands, for which IR/X can be determined directly. A comparison of these sources is shown in Figure 8. For the eighteen sources detected in both bands (shaded histogram), nearly all (80%) have $\text{IR}/\text{X} \leq 0.2$, indicating a relatively unobscured AGN. For sources detected by Chandra but not MIPS, IR/X upper-limits were determined as $0.3 \text{ mJy}/(\text{F}_{0.5-2.0\text{keV}})$ with the “soft” X-ray flux in units of $10^{-16} \text{ erg s}^{-1} \text{ cm}^{-2}$. For sources detected only at $24 \mu\text{m}$, we calculated lower-limits to IR/X using $\text{F}_{24\mu\text{m}}$ in mJy divided by 1.5. Figure 8 shows a clear separation between the sources detected only by MIPS or Chandra, with the former being identified with starburst or obscured AGN dominated systems and the latter with unobscured AGN. Quantitatively, 90% of the Chandra-only detections have $\text{IR}/\text{X} < 0.2$. Similarly, 90% of the MIPS-only detections have $\text{IR}/\text{X} > 0.2$. These results apply to the full sample in the overlapping area, virtually all of which have optical identifications, and indicate that the great majority of X-ray sources are powered by AGN.

5. Discussion

5.1. Space Densities Of The OIRS And OIXS Populations

We of course have no direct measure of the redshifts for the OIRS population. However the requirement that they be optically “invisible” likely forces the majority to be at $z \gtrsim 1$. Supporting evidence for this comes from IRS spectroscopy of a sample of sixteen optically faint and invisible MIPS sources in Boötes with $\text{F}_{24\mu\text{m}} \geq 0.75 \text{ mJy}$ in Houck et al. (2005). For the ten optically invisible infrared sources, the median spectroscopic redshift was 2.1, with only one object having a redshift less than one, and that at $z = 0.7 \pm 0.1$. We can calculate rough estimates of the OIRS space density by assuming that they lie within certain broad

redshift ranges. By comparing these with measured or estimated space densities of other extragalactic objects (see Table 5) we can gain additional clues into their nature. Arguments based on surface density comparisons are subject to various complexities and assumptions (i.e., the OIRS redshift range) that are difficult to take into account. Nevertheless, such an approach is still informative.

The average surface density of the 27 OIRSs with no MIPS detections, sources whose emission is likely to be dominated by an AGN, is $\sigma_{\text{OIRS}} = 80 \pm 15 \text{ deg}^{-2}$. For our adopted flat Λ CDM cosmology and H_0 , this corresponds to a mean space density $\rho_{\text{OIRS}} = (2.4 \pm 0.5) \times 10^{-6} \text{ Mpc}^{-3}$ over a $1 < z < 5$ redshift range. This is much smaller than the space density of current day massive ellipticals ($\rho_{\text{elliptical}} \sim 10^{-3} \text{ Mpc}^{-3}$, Marzke et al. 1994), though comparable to that of local radio galaxies ($\rho_{\text{RG}} \sim 10^{-6} \text{ Mpc}^{-3}$, Osterbrock 1989).

This can also be compared with the space density of bright ($M_B < -26$) quasars over $0.4 < z < 5$ shown in Figure 3 of Fan et al. (2001), which combines results from 2dF (Boyle et al. 2000), Warren et al. (1994), and Schmidt et al. (1995), as well as the Sloan Digital Sky Survey. The OIRS space density is considerably larger than that of bright optically selected quasars, even at $z \sim 2.5$ where the quasar distribution peaks ($\rho_{\text{qso}} \sim 5 \times 10^{-7} \text{ Mpc}^{-3}$). The discrepancy is much larger at lower and higher redshifts. For example, from $z = 3-5$ the bright quasar space density drops from $\sim 2 \times 10^{-7}$ to $\sim 1 \times 10^{-8} \text{ Mpc}^{-3}$, which is smaller than the OIRS space density by one and two orders of magnitude, respectively.

However, the OIRSs are almost certainly less luminous optically than $M_B = -26$. Assuming a power law form for the optical continuum of $f_\nu \propto \nu^{-0.5}$, the B_W upper limit of ~ 26.5 implies absolute magnitude upper limits of approximately $M_B = -18$ to -23 for $z=1-5$. These values are less than or equal to $M_B = -23$, the traditional boundary between Seyfert galaxies and quasars. The cumulative luminosity function for optically selected quasars at $z > 3.6$ in Fan et al. (2001) is,

$$\log\Phi(z, < M_B) = (-6.91 \pm 0.19) - (0.48 \pm 0.15)(z - 3) + (0.63 \pm 0.10)(M_B + 26) \quad (2)$$

in units of Mpc^{-3} . This equation is strictly valid for $M_B < -25.6$, and employing it for intrinsically fainter objects requires that the luminosity function's slope does not change significantly, which we admit is an assumption. Nevertheless, using Equation 2 to calculate the space density of objects at $z = 5$ with $-23 < M_B < -22$ gives a value of $\rho = 3 \times 10^{-6} \text{ Mpc}^{-3}$, which is similar to the mean OIRS space density. For the same range in M_B , we derive space densities of 3×10^{-5} and $1 \times 10^{-5} \text{ Mpc}^{-3}$ at redshifts of three and four, respectively. At a redshift of two, the 2dF cumulative luminosity function shown in Equation 4 of Fan et al. (2001) gives $\rho = 1 \times 10^{-6} \text{ Mpc}^{-3}$ for $M_B < -25.5$. For a range in M_B from -25 to -24 the extrapolated space density would be $\sim 3 \times 10^{-6} \text{ Mpc}^{-3}$, which is also similar to the mean ρ for the OIRS population. Thus, within the uncertainties accrued by extrapolating the

bright high- z quasar luminosity function to $M_B \sim -21$, we conclude that the averaged space density of OIRSs is consistent with that of lower luminosity AGN with redshifts $2 < z < 5$. Moreover, the distribution of q values for the OIRS population clearly implies a strong radio-loud AGN component.

The average space density of sub-mm galaxies provides another point of comparison. These objects are thought to be the progenitors of massive bulges that are powered primarily by heavily obscured star formation. Taking the sources detected at $850 \mu\text{m}$ by Barger et al. (1999) with fluxes greater than 2.2 mJy and assuming they lie between $1 < z < 3$ would result in a space density of $\rho_{850\mu\text{m}} = 7 \times 10^{-5} \text{ Mpc}^{-3}$. This would be nearly sixteen times larger than the average OIRS space density over the same redshift interval, which we determine to be $\rho_{\text{OIRS}} = (4.1 \pm 0.8) \times 10^{-6} \text{ Mpc}^{-3}$ if all OIRSs are within this interval. The sub-mm galaxies have a substantially larger space density. The discrepancy becomes even worse if one extrapolates the $850 \mu\text{m}$ source counts to fainter sources in order to account for the diffuse sub-mm background emission, in which case the average space density of sub-mm sources becomes comparable to the space density of present-day elliptical galaxies. Such a large difference in space density suggests that the OIRSs are not the objects that make up the sub-mm source population.

The average surface density of the eleven OIXSs is $157 \pm 47 \text{ deg}^{-2}$. While formally $\sim 50\%$ larger than that of the OIRS population determined in §4.1, $\sigma_{\text{OIXS}} \approx \sigma_{\text{OIRS}}$ given the uncertainties. In §4.3 we argued that nine out of eleven are likely to have $1 < z < 5$ based on their X-ray hardness ratios. Distributing these uniformly over this redshift range gives an average space density $\rho_{\text{OIXS}} = (3.9 \pm 1.3) \times 10^{-6} \text{ Mpc}^{-3}$, again comparable to ρ_{OIRS} . Thus the conclusions reached above for the OIRS population holds for OIXSs as well: ρ_{OIXS} is larger than the space density of local radio galaxies and luminous optically selected $1 < z < 5$ quasars, but consistent with the space density of lower luminosity AGN ($M_B > -23$) extrapolated from the quasar luminosity function of Fan et al. (2001). If four of the OIXSs are at $z \sim 4-5$ as is suggested by the HR values in Table 3 and Figure 6, then the OIXS space density over $1 < z < 3$ can not be larger than $(3.3 \pm 1.5) \times 10^{-6} \text{ Mpc}^{-3}$, which is more than an order of magnitude smaller than the mean space density of Barger et al.’s (1999) $F_{850\mu\text{m}} > 2.2 \text{ mJy}$ sub-mm sources. OIXSs do not appear to be the sources making up the sub-mm galaxy population.

While additional and independent observational evidence is clearly required to place these conclusions on a more solid footing, the estimated space densities of both OIRSs and OIXSs are consistent with lower luminosity AGN hosts ($M_B \gtrsim -23$) at $z \sim 1-5$, suggesting that we are seeing the fainter end of the high redshift quasar luminosity function.

5.2. Do The Optically Invisible Radio And X-Ray Sources Represent Different Populations Of AGN?

We concluded in §4.2 that the OIRSs are predominately AGN because of their 24 μm to 20 cm flux ratios, and we concluded in §4.3 that the OIXSs are likewise primarily AGN because of their low infrared to X-ray flux ratios. It is worth noting that these two independently derived samples of optically invisible AGN do not overlap. In the common radio and X-ray survey region (Table 4) there are 10 OIRSs, none of which are detected in “soft” or “hard” X-ray bands by Wang et al. (2004). Similarly, there are 14 OIXSs within our VLA survey. None of these are detected at 20 cm.

We can ask whether this result is consistent with expectations from previous deep parallel surveys at radio and X-ray wavelengths. The most relevant study is that of Bauer et al. (2003) of the Chandra Deep Field North, which compared radio and X-ray sources at flux levels comparable to our sample. They used a variety of spectroscopic indicators, including optical and X-ray spectra to identify AGN. Their results showed that such AGN covered a wide range of X-ray to radio flux ratio. Specifically, they found (their Figure 1) that AGN could exist with $0.002 < F_{\text{X-ray}}/F_{20\text{cm}} < 2.5$, where $F_{\text{X-ray}}$ is the Chandra full-band flux in units of $10^{-16} \text{ ergs s}^{-1} \text{ cm}^{-2}$ and $F_{20\text{cm}}$ is in units of μJy . The upper bound could even exceed 2.5 as this value derives from the upper limit of 40 μJy for the radio sources not detected in X-rays. From this, given that the faintest full-band X-ray flux in Wang et al. (2004)’s survey is $5 \times 10^{-16} \text{ erg s}^{-1} \text{ cm}^{-2}$, an AGN could have a 20 cm flux density as high as ~ 2 mJy and still not be detected in X-rays. Of our OIRS sample, only a source like #362 with $F_{20\text{cm}} = 6.7 \text{ mJy}$ would have been easily detected in X-rays. The OIRSs’ median 20 cm flux density is 400 μJy . For such a source to have a full-band X-ray flux less than $5 \times 10^{-16} \text{ erg s}^{-1} \text{ cm}^{-2}$ would imply $F_{\text{X-ray}}/F_{20\text{cm}} < 0.013$, which is well within the possible range found by Bauer et al. (2003).

Conversely, the median OIXS has full band X-ray flux of $5 \times 10^{-15} \text{ ergs s}^{-1} \text{ cm}^{-2}$. In order not to be detected in our radio survey, it would have to be fainter than 100 μJy , or have $F_{\text{X-ray}}/F_{20\text{cm}} > 0.5$, which is also well within the observed range of this ratio. We conclude, therefore, that the lack of overlap between the radio and X-ray samples of optically invisible AGN is consistent with the wide range of $F_{\text{X-ray}}/F_{20\text{cm}}$ that has been established among AGN.

6. Summary

We have combined a Spitzer/MIPS survey of the NDWFS Boötes field at $24\ \mu\text{m}$ with an A-array VLA 20 cm survey of a $0.5\ \text{deg}^2$ subregion and a 172 ks Chandra observation to investigate the nature of optically “invisible” radio and X-ray sources. These we define to be compact radio and X-ray sources without visible counterparts in the NDWFS B_W , R , & I images. It has been proposed that these objects represent populations of high redshift galaxies harboring heavily obscured starbursts or AGN. From the VLA and Chandra surveys we identify 31 OIRSs and 12 OIXSs within the area surveyed by MIPS at $24\ \mu\text{m}$, out of total radio and X-ray source populations of 377 and 168, respectively. Only four of the 31 OIRSs and none of the OIXSs are detected by MIPS at $24\ \mu\text{m}$. We compared the 20 cm and $24\ \mu\text{m}$ emission properties of the OIRSs observed with MIPS with those expected from late spiral, ULIRG, Seyfert, and quasar SEDs over a wide redshift range. We conclude that the OIRSs are primarily a population of galaxies powered by AGN rather than dust enshrouded starbursts, and that they likely lie at $z > 1$. Likewise, of the OIXSs with measured “soft” X-ray fluxes, all have $24\ \mu\text{m}$ to 0.5-2 keV band flux ratio limits consistent with a dominant and relatively unobscured AGN. The X-ray properties of OIXSs suggest that most are likely at $z > 1$, with several possibly at $z \sim 4$. Given the wide range in X-ray and radio properties of AGN, the fact that the OIRSs and OIXSs have no object in common does not rule out their being from the same AGN source population.

Assuming the OIRSs populate the redshift range $1 < z < 5$, their average space density is $(2.4 \pm 0.5) \times 10^{-6}\ \text{Mpc}^{-3}$. This is consistent with the space densities derived using the cumulative quasar luminosity function from Fan et al. (2001) over the redshift range $z = 2-5$ for $-23 < M_B < -22$, i.e., AGN with blue luminosities comparable to current epoch Seyfert galaxies. The space density of $850\ \mu\text{m}$ sources is much larger than this, suggesting that they are a fundamentally different class of object. Similarly, the OIXSs have an average space density of $(3.8 \pm 1.2) \times 10^{-6}\ \text{Mpc}^{-3}$ if they exist uniformly throughout the redshift range $1 < z < 5$, which is similar to the OIRSs’. This is also consistent with the space density of lower luminosity AGN extrapolated from Fan et al. (2001) for this redshift range.

We would like to thank Keven Xu for access to his library of galaxy spectral energy distributions, and both Robert Becker and David Helfand for valuable discussions. We also wish to thank the referee for suggestions that led to improvements in the manuscript. This work is based in part on observations made with the Spitzer Space Telescope, which is operated by the Jet Propulsion Laboratory, California Institute of Technology under NASA contract 1407. Support for this work was provided by NASA through Contract Number 1257184 issued by JPL/Caltech. The National Radio Astronomy Observatory is a facility of the Na-

tional Science Foundation operated under cooperative agreement by Associated Universities, Inc. This publication made use of photographic data from the National Geographic Society – Palomar Observatory Sky Survey (NGS-POSS) obtained using the Oschin Telescope on Palomar Mountain. The NGS-POSS was funded by a grant from the National Geographic Society to the California Institute of Technology. The plates were processed into the present compressed digital form with their permission. The Digitized Sky Survey was produced at the Space Telescope Science Institute under US Government grant NAG W-2166. This research has also made use of the NASA/IPAC Extragalactic Database (NED) which is operated by the Jet Propulsion Laboratory, California Institute of Technology, under contract with the National Aeronautics and Space Administration.

REFERENCES

- Appleton, P. et al. 2004, *ApJS*, 154, 147
- Baars, J. W., Genzel, R., Pauliny-Toth, I., & Witzel, A. 1977, *A&A*, 61, 99
- Barger, A., Cowie, L., Capak, P., Alexander, D., Bauer, F., Fernandez, E., Brandt, W., Garmire, G., & Hornschemeier, A. 2003, *AJ*, 126, 632
- Bauer, F., Alexander, D., Brandt, W., Hornschemeier, A., Vignali, C., Garmire, G., & Schneider, D. 2003, *AJ*, 126, 632
- Becker, R., White, R., & Helfand, D. 1995, *ApJ*, 450, 559
- Bell, E. F. 2003, *ApJ*, 586, 794
- Bertin, E. & Arnouts, S. 1996, *A&AS*, 117, 393
- Boyle, B. J., Shanks, T., Croom, S. M., Smith, R. J., Miller, L., Loaring, B., & Heymans, C. 2000, *MNRAS*, in press (astro-ph/0005368)
- Chary, R., & Elbaz, D. 2001, *ApJ*, 556, 562
- de Vries, W. H., Morganti, R., Röttgering, H. J., Vermeulen, R., van Breugel, W., Rengelink, R., & Jarvis, M. J. 2002, *AJ*, 123, 1784
- Fan, X. et al. 2001, *AJ*, 121, 54
- Fomalont, E., Kellermann, K., Partridge, R., & Richards, E. 2002 *AJ*, 123, 2402
- Haarsma, D. B., Partridge, R. B., Windhorst, R. A., & Richards, E. A. 2001, astro-ph 0007315
- Helou, G., Soifer, B. T., & Rowan-Robinson, M. 1985, *ApJ*, 298, L7
- Higdon, S. J. U., Weedman, D. W., Higdon, J. L., Herter, T. L., Charmandaris, V., Houck, J. R., Hao, L., Brandl, B., Armus, L., & Soifer, B. T. 2004, *ApJS*, 154, 178
- Hopkins, A., Alfonso, J., Cram, L., & Mobasher, B. 1999, *ApJ*, 519, L59
- Houck, J. R. et al. 2004, *ApJ*, 154, L18
- Houck, J. R., Soifer, B. T., Weedman, D., Higdon, S. J. U., Higdon, J. L., Brown, M., Dey, A., Jannuzi, B., Le Floch, E., Rieke, M., Armus, L., Charmandaris, V., Brandle, B., & Teplitz, H. 2005, *ApJ*, in press

- Jannuzi, B. & Dey, A. 1999, ASP Conference Series Vol. 191, (R. Weymann, L. Storrie-Lombardi, M. Sawicki, & R. Brunner, eds.), p. 111
- de Jong, T., Klein, U., Wielbinski, R., & Wunderlich, E. 1985, A&A, 147, L6
- Lagache, G., Dole, H., & Puget, J. 2003, MNRAS, 338, 555
- Papovich, C., Dole, H., Egami, E., Le Floc'h, Perez-Gonzalez, P., Gai, L., Beichman, C., Blaylock, M., Engelbracht, C., Gordon, K., Hines, D., Misselt, K., Morrison, J., Mould, J., Muzerolle, J., Neugebauer, G., Richards, P., Rieke, G., Rieke, M., Rigby, J., Su, K., & Young, E. 2004, ApJS, 154, 70
- Rhoads, J. et al. 2000, ApJ, 545, L85
- Richards, E. A., Fomalont, E. B., Kellermann, K. I., Windhorst, R. A., Partridge, R. B., Cowie, L. L., & Barger, A.J. 1999, ApJ, 526, L73
- Rieke, G. H. et al. 2004, ApJ, 154, L25
- Schneider, D. P., Schmidt, M., & Gunn, J. E. 1991, AJ, 101, 2004
- Wang, J. X., Malhotra, S., Rhoads, J., Brown, M., Dey, A., Heckman, T., Jannuzi, B., Norman, C., Tiede, G., & Tozzi, P. 2004, AJ, 127, 213
- Warren, S. J., Hewett, P., & Osmer, P. S. 1994, ApJ, 421, 412
- Weedman, D., Charmandaris, V., & Zezas, A. 2004, ApJ, 600, 106
- Werner, M. W. et al. 2004, ApJ, 154, L1
- Xu, C., Lonsdale, C. J., Shupe, D. L., O'Linger, J., & Masci, F. 2001, ApJ, 562, 179
- Yun, M., Reddy, N., & Condon, J. 2001, ApJ, 554, 803

Table 1: VLA Observing Parameters

| | | | |
|--|----------------------------|-------------|-------------|
| Observing Dates: | 26, 27 June & 27 July 2003 | | |
| Array Configuration: | A | | |
| Min./Max. Baseline (km): | 0.68/36.4 | | |
| Number of Antennas: | 27 | | |
| Primary Beam FWHM (arcmin): | 31.5 | | |
| IF Frequencies (GHz): | 1.3649 & 1.4351 | | |
| Number of Channels per IF: | 7 | | |
| Channel Separation (MHz): | 3.125 | | |
| Effective Bandwidth (MHz): | 43.750 | | |
| Phase & Gain Calibrator: | 1416+347 | | |
| Flux & Bandpass Calibrator: | 3C 48 | | |
| Synthesized Beam FWHM (arcsec): ^a | 1.4 | | |
| Field Centers | North | East | South |
| R.A. (J2000): | 14:25:57.00 | 14:27:27.00 | 14:25:57.00 |
| Dec. (J2000): | 35:32:00.0 | 35:17:12.0 | 35:02:24.0 |
| Time on Source (hrs): | 5.5 | 4.9 | 5.4 |
| Map r.m.s. (μ Jy/beam): | 14.8 | 15.5 | 15.6 |

^aRobust weighting.

Table 2. Optically Invisible Radio Sources In the Boötes Sub-Region

| Radio ID# | Source | $F_{20\text{cm}}^{(a)}$ (μJy) | $F_{20\text{cm}}^{\text{peak}}$ (μJy) | $a \times b$ (arcsec) | ϕ (deg.) | $F_{24\mu\text{m}}^{(b)}$ (μJy) | $q^{(c)}$ | $B_W^{(d)}$ | $R^{(d)}$ | $I^{(d)}$ |
|-----------|---------------------|---|---|--------------------------|------------------|---|------------------|-------------|-----------|-----------|
| 9 | J142822.75+351849.8 | 511 ± 62 | 128 | 3.5×2.7 | 70 | ... | < -0.26 | > 27.2 | > 25.3 | > 25.1 |
| 19 | J142813.97+351136.6 | 565 ± 36 | 378 | 1.9×1.5 | 126 | ... | < -0.30 | > 27.1 | > 25.2 | > 24.5 |
| 22 | J142810.60+350659.2 | 308 ± 42 | 125 | 1.7×1.5 | 128 | ... | < -0.04 | > 26.9 | > 24.9 | > 24.3 |
| 49 | J142744.94+352616.5 | 565 ± 32 | 378 | 1.9×1.5 | 126 | ... | < -0.30 | > 27.2 | > 25.3 | > 25.0 |
| 52 | J142740.39+350117.5 | 240 ± 38 | 148 | 2.2×1.4 | 137 | ... | < 0.07 | > 26.9 | > 25.3 | > 24.2 |
| 79 | J142713.75+352134.5 | 948 ± 37 | 602 | 2.1×1.5 | 137 | ... | < -0.53 | > 26.8 | > 25.2 | > 25.3 |
| 92 | J142702.54+351215.2 | 239 ± 34 | 210 | 1.5×1.4 | 49 | ... | < 0.07 | > 27.1 | > 25.6 | > 24.7 |
| 97 | J142701.06+351949.3 | 396 ± 32 | 271 | 1.7×1.6 | 69 | 234 ± 44 | -0.24 ± 0.21 | > 27.2 | > 25.8 | > 25.2 |
| 110 | J142652.98+353351.1 | 177 ± 30 | 162 | 1.8×1.3 | 129 | ... | < 0.20 | > 27.1 | > 26.1 | > 25.5 |
| 114 | J142650.00+350711.0 | 372 ± 47 | 164 | 2.4×1.8 | 40 | ... | < -0.12 | > 26.8 | > 25.5 | > 25.0 |
| 156 | J142632.14+353614.2 | 799 ± 59 | 262 | 2.9×2.0 | 164 | ... | < -0.46 | > 27.0 | > 26.0 | > 25.4 |
| 176 | J142624.94+350614.6 | 249 ± 35 | 171 | 1.9×1.5 | 14 | 462 ± 44 | 0.27 ± 0.17 | > 27.0 | > 25.5 | > 24.7 |
| 182 | J142623.40+345821.1 | 554 ± 39 | 352 | 2.1×1.6 | 100 | ... | < -0.30 | > 27.0 | > 25.7 | > 24.7 |
| 185 | J142621.92+353114.7 | 327 ± 35 | 230 | 1.6×1.6 | 131 | ... | < -0.07 | > 27.0 | > 26.0 | > 25.2 |
| 208 | J142613.81+353154.4 | 189 ± 33 | 145 | 1.6×1.5 | 76 | ... | < 0.17 | > 27.0 | > 26.0 | > 25.3 |
| 209 | J142613.53+352810.9 | 165 ± 31 | 77 | 2.0×1.4 | 12 | ... | < 0.23 | > 27.0 | > 25.9 | > 25.3 |
| 232 | J142605.13+350604.2 | 512 ± 18 | 404 | 1.6×1.5 | 88 | ... | < -0.26 | > 26.9 | > 25.1 | > 24.7 |
| 245 | J142602.35+350907.9 | 244 ± 29 | 230 | 1.6×1.3 | 2 | 440 ± 52 | 0.26 ± 0.17 | > 26.9 | > 25.2 | > 24.8 |
| 278 | J142551.58+351543.2 | 445 ± 70 | 118 | 2.6×2.3 | 178 | ... | < -0.20 | > 27.1 | > 25.8 | > 25.6 |
| 282 | J142550.49+352935.4 | 155 ± 30 | 77 | 2.3×1.5 | 19 | ... | < 0.26 | > 27.2 | > 26.0 | > 25.3 |
| 305 | J142544.84+351702.2 | 777 ± 83 | 165 | 3.4×2.6 | 77 | ... | < -0.44 | > 26.9 | > 26.2 | > 25.2 |
| 313 | J142543.00+353049.2 | 1165 ± 71 | 296 | 3.0×2.6 | 11 | ... | < -0.62 | > 27.1 | > 25.8 | > 25.2 |
| 323 | J142537.12+345229.2 | 181 ± 35 | 126 | 1.7×1.3 | 20 | ... | < 0.19 | > 27.1 | > 25.5 | > 25.0 |
| 346 | J142528.98+352824.8 | 367 ± 36 | 205 | 2.0×1.7 | 21 | ... | < -0.12 | > 27.0 | > 26.1 | > 25.4 |
| 349 | J142527.24+352649.7 | 241 ± 47 | 108 | 2.5×1.7 | 80 | ... | < 0.07 | > 27.1 | > 25.9 | > 25.1 |
| 362 | J142525.04+344913.2 | 6738 ± 69 | 1806 | 3.0×2.3 | 44 | ... | < -1.38 | > 27.0 | > 25.8 | > 24.9 |
| 363 | J142524.84+352554.1 | 145 ± 38 | 90 | 2.1×1.5 | 38 | 328 ± 52 | 0.35 ± 0.31 | > 27.2 | > 25.9 | > 25.3 |

Table 2—Continued

| Radio ID# | Source | $F_{20\text{cm}}^{(a)}$ (μJy) | $F_{20\text{cm}}^{\text{peak}}$ (μJy) | $a \times b$ (arcsec) | ϕ (deg.) | $F_{24\mu\text{m}}^{(b)}$ (μJy) | $q^{(c)}$ | $B_W^{(d)}$ | $R^{(d)}$ | $I^{(d)}$ |
|-----------|---------------------|---|---|--------------------------|------------------|---|-----------|-------------|-----------|-----------|
| 375 | J142519.91+352417.8 | 847 ± 50 | 346 | 2.5×1.9 | 42 | ... | <-0.48 | >26.9 | >26.0 | >25.4 |
| 380 | J142516.19+350248.1 | 1906 ± 40 | 1070 | 2.0×1.7 | 79 | ... | <-3.83 | >26.9 | >25.5 | >24.9 |
| 388 | J142508.28+353901.9 | 180 ± 34 | 111 | 2.3×1.3 | 56 | ... | < 0.19 | >27.1 | >26.0 | >25.3 |
| 389 | J142507.78+354210.4 | 302 ± 21 | 164 | 2.1×1.7 | 116 | ^(e) ... | ... | >26.9 | >26.1 | >25.3 |
| 393 | J142506.41+353813.4 | 171 ± 14 | 112 | 2.2×1.4 | 125 | ^(e) ... | ... | >27.0 | >25.8 | >25.2 |
| 410 | J142457.20+351620.5 | 875 ± 75 | 307 | 2.9×1.9 | 151 | ... | <-0.49 | >27.0 | >25.8 | >25.3 |
| 430 | J142445.36+353417.1 | 1410 ± 62 | 423 | 3.3×1.9 | 102 | ^(e) ... | ... | >27.0 | >25.9 | >25.2 |
| 434 | J142444.01+351227.1 | 588 ± 47 | 262 | 3.1×1.4 | 75 | ^(e) ... | ... | >27.0 | >25.5 | >24.7 |
| 441 | J142435.59+351046.2 | 1486 ± 59 | 484 | 2.7×2.2 | 11 | ^(e) ... | ... | >26.5 | >25.1 | >24.4 |

^(a)Integrated 20 cm flux in μJy .

^(b)Integrated 24 μm fluxes (or non-detection) at radio source position.

^(c) $q = \log(F_{24\mu\text{m}}/F_{20\text{cm}})$.

^(d) B_W , R , & I limits (5σ) calculated in $2''$ diameter apertures centered on the OIRS positions. See §4.1.

^(e)These OIRSs are outside the MIPS 24 μm survey area.

Table 3. Optically Invisible X-Ray Sources

| X-Ray ^(a) ID # | Source | F _{0.5–2keV} ^(b) | HR ^(c) | IR/X ^(d) | B _W ^(e) | R ^(e) | I ^(e) |
|------------------------------|---------------------|--------------------------------------|---|---------------------|-------------------------------|------------------|------------------|
| 9 | J142539.55+353357.9 | 6.9 | -0.43 ^{+0.19} _{-0.17} | <0.04 | >26.8 | >25.9 | >25.3 |
| 15 | J142530.71+353911.3 | 11.9 | 0.12 ^{+0.11} _{-0.11} | <0.03 | >27.1 | >25.8 | >25.4 |
| 31 | J142555.40+353650.4 | 3.3 | -0.56 ^{+0.33} _{-0.25} | <0.08 | >26.9 | >25.8 | >25.3 |
| 51 | J142546.33+353349.4 | <1.5 ^(f) | >0.56 | ... | >27.0 | >26.0 | >25.3 |
| 69 | J142531.17+353921.6 | <1.5 ^(f) | >0.73 | ... | >26.9 | >26.2 | >25.3 |
| 70 | J142530.63+353420.3 | 9.4 | -0.42 ^{+0.16} _{-0.14} | <0.03 | >27.0 | >25.9 | >25.3 |
| 73 | J142526.68+353140.8 | 7.0 | -0.13 ^{+0.19} _{-0.18} | <0.04 | >27.0 | >26.0 | >25.3 |
| 96 | J142558.13+353216.1 | 3.8 | -0.33 ^{+0.30} _{-0.26} | <0.08 | >26.9 | >25.8 | >25.3 |
| 103 | J142544.20+354018.4 | <1.5 ^(f) | >0.86 | ... | >26.9 | >25.9 | >25.4 |
| 112 | J142527.59+354012.1 | 3.2 | 0.10 ^{+0.25} _{-0.26} | <0.09 | >27.1 | >25.8 | >25.2 |
| 120 | J142522.40+353517.2 | <1.5 ^(f) | >0.40 | ... | >26.9 | >25.8 | >25.2 |

^(a)X-ray source number from Table 1 in Wang et al. (2004).

^(b)Integrated “Soft” (0.5-2.0 keV) band flux in units of 10^{-16} erg s⁻¹ cm⁻² from Wang et al. (2004).

^(c)X-ray “hardness” ratio from Wang et al. (2004). HR = (H - S)/(H + S), where H and S are the “hard” (2-7 keV) and “soft” (0.5-2 keV) band counts.

^(d)The 24 μ m to soft X-ray flux ratio, in units of mJy/(10^{-16} erg s⁻¹ cm⁻²).

^(e)B_W, R, & I limits (5 σ) calculated in 2'' diameter apertures centered on the OIXS positions as in §4.1.

^(f)OIXSs #51, 69, 103 & 120 were only detected in the Chandra “hard” or “total” bands, and not the 0.5-2 keV “soft” band. Their positional accuracies are all < 1''.

Table 4: Source Detection Statistics In Radio and X-ray Surveys

| Radio Survey | Total Number | $\sigma^{(a)}$ | %MIPS ^(b) | %Radio ^(c) | |
|-----------------------------|--------------------|--------------------|----------------------|-----------------------|-----------------------|
| MIPS Sources (> 0.3 mJy) | 1405 | 2810 ± 75 | ... | 9 | |
| Compact Radio Sources | 377 | 754 ± 39 | 33 | ... | |
| OIRSs | 36 | $104 \pm 17^{(d)}$ | 13 ^(e) | ... | |
| X-Ray Survey | Total Number | $\sigma^{(a)}$ | %MIPS | %Radio | %X-ray ^(f) |
| X-Ray Sources | 104 ^(g) | 1486 ± 146 | 17 | 11 | ... |
| MIPS Sources (> 0.3 mJy) | 240 | 3429 ± 221 | ... | 11 | 8 |
| Compact Radio Sources | 73 | 1043 ± 123 | 36 | ... | 14 |
| OIXSs | 11 | 157 ± 47 | 0 | 0 | ... |
| OIRSs | 8 | 114 ± 40 | 13 | ... | 0 |

^(a)Average surface density in deg^{-2} .

^(b)Percent of sources detected at $24 \mu\text{m}$ by MIPS.

^(c)Percent of sources detected at 20 cm.

^(d)Surface density for all 36 OIRSs, including those outside the MIPS survey area.

^(e)Percentage of the 31 OIRSs observed by MIPS that were detected at $24 \mu\text{m}$.

^(f)Percent of sources detected in Chandra 0.5-2.0 keV band by Wang et al. (2004).

^(g)Number of X-ray sources observed by MIPS at $24 \mu\text{m}$.

Table 5. Average Space Density Comparison

| Objects | ρ (10^{-6} Mpc 3) | Redshift | Notes |
|----------------|----------------------------------|-------------|--|
| OIRS | 3.1 ± 0.5 | $1 < z < 5$ | Calculated using all 36 OIRSs in the VLA survey. |
| | 2.4 ± 0.5 | $1 < z < 5$ | Calculated using the 27 OIRSs not detected by MIPS. |
| | 4.1 ± 0.8 | $1 < z < 3$ | |
| OIXS | 4.7 ± 1.4 | $1 < z < 5$ | Calculated using all 11 OIXSs in Chandra survey. |
| | 3.9 ± 1.3 | $1 < z < 5$ | Calculated using the 9 OIXSs with $HR < 0.6$. |
| | 3.3 ± 1.5 | $1 < z < 3$ | Calculated using the 5 OIXSs with $-0.5 < HR < 0.6$. |
| Ellipticals | 10^3 | ~ 0 | Local massive ellipticals (Marzke et al. 1994). |
| Radio Galaxies | ~ 1 | ~ 0 | Local radio galaxies (Osterbrock 1989). |
| Sub-mm Sources | 70 | $1 < z < 3$ | $F_{850\mu\text{m}} > 2.2$ mJy (Barger et al. 1999). |
| Bright QSOs | 0.01 | $z = 1$ | $M_B < -26$ QSOs. From Figure 3 in Fan et al. (2001). |
| | 0.5-0.01 | $2 < z < 5$ | $M_B < -26$ QSOs. From Figure 3 in Fan et al. (2001). |
| Faint QSOs | 30-3 | $3 < z < 5$ | $-23 < M_B < -22$ QSOs. Extrapolated from Fan et al. (2001). |

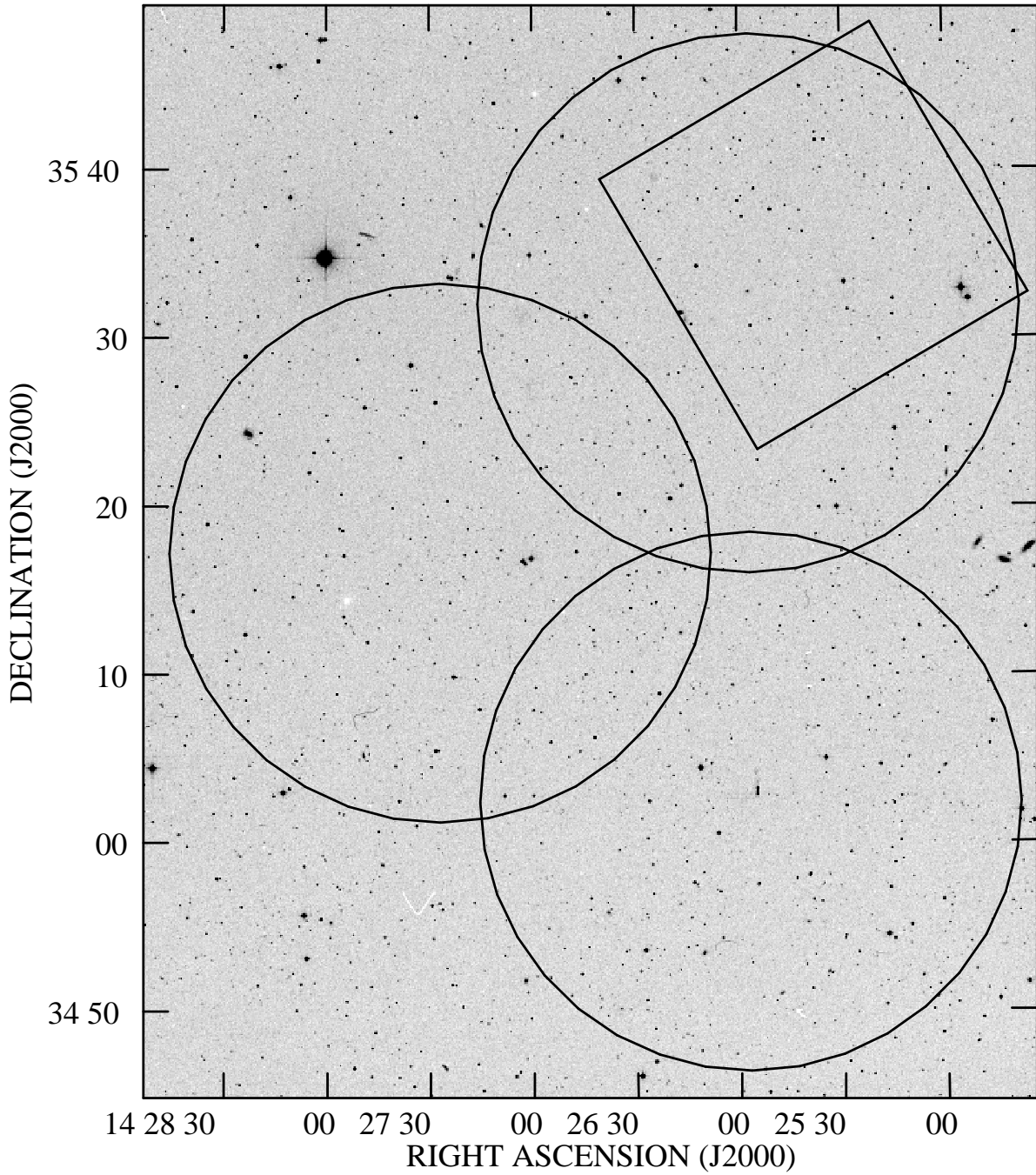


Fig. 1.— The survey fields. The circles represent the VLA primary beam FWHM ($32'$) for the three array pointings (North, East, & South), while the square represents the region observed with Chandra by Wang et al. (2004). These are superposed on a DPOSS grey-scale image.

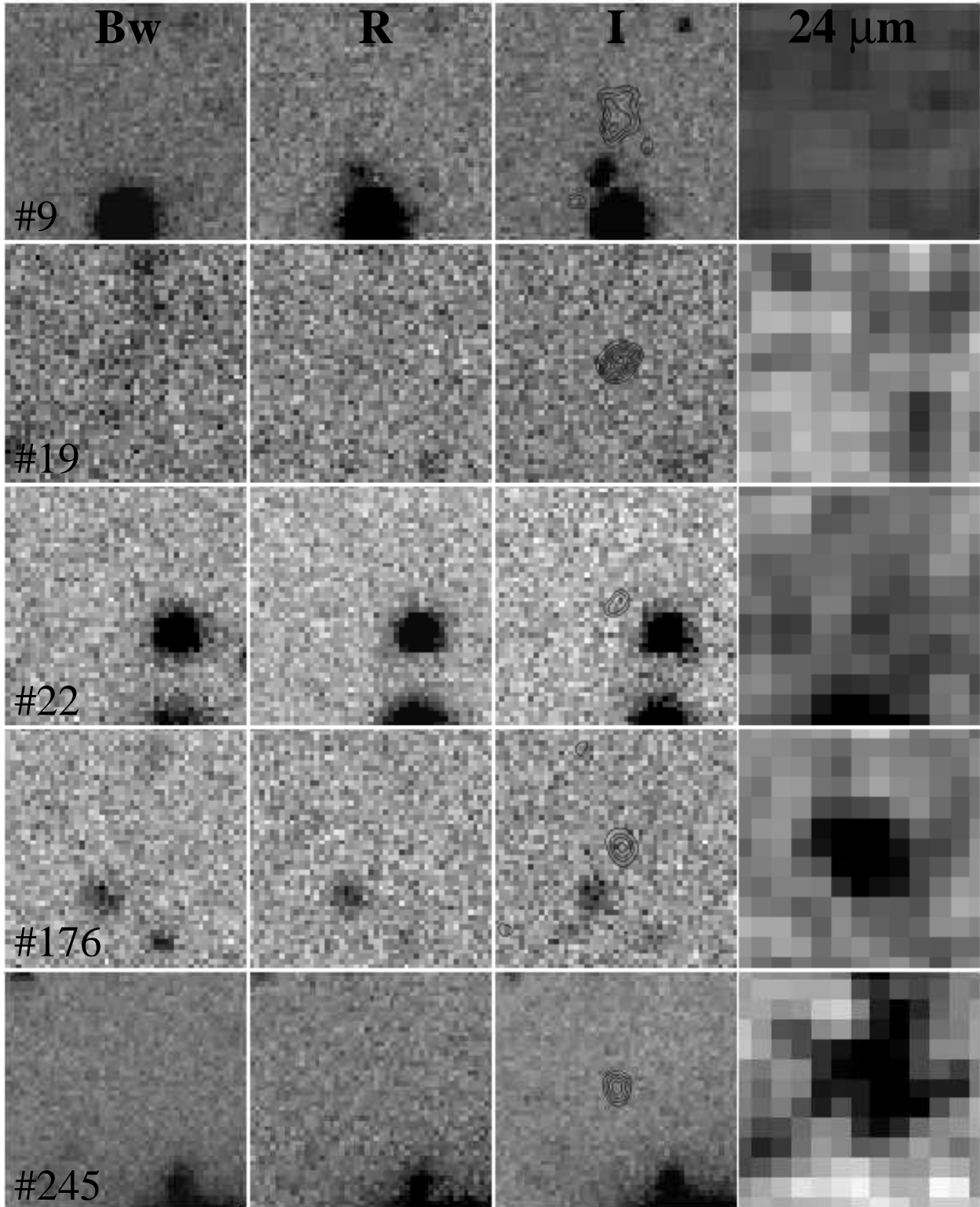


Fig. 2.— A sample of five optically invisible radio sources (OIRSs) shown in optical B_W , R , I and MIPS $24\ \mu\text{m}$ bands. Radio contours are shown superposed on the I image, with the lowest contour representing the local $3\ \sigma$ level. Each field is $12'' \times 12''$.

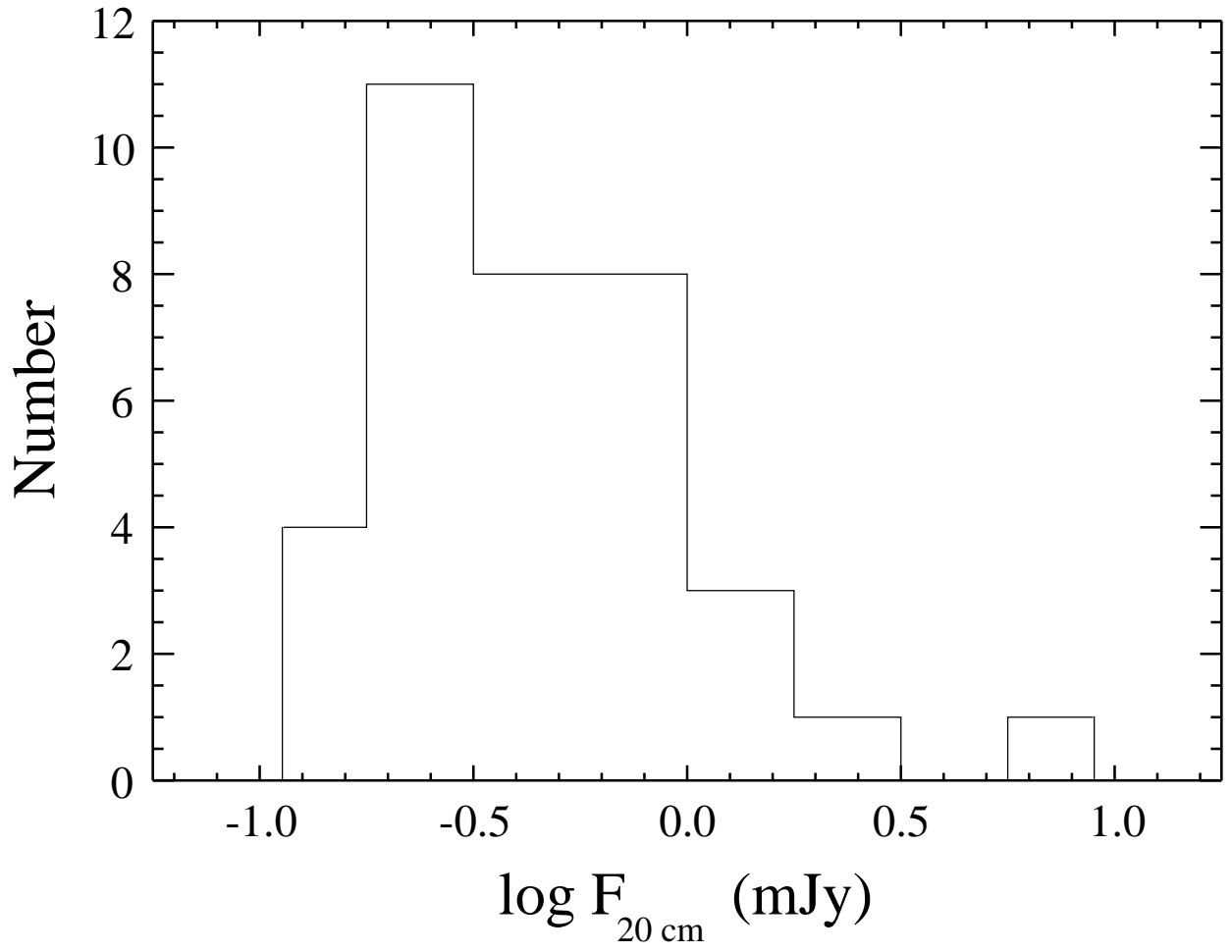


Fig. 3.— Histogram of 20 cm flux densities for the OIRS sample.

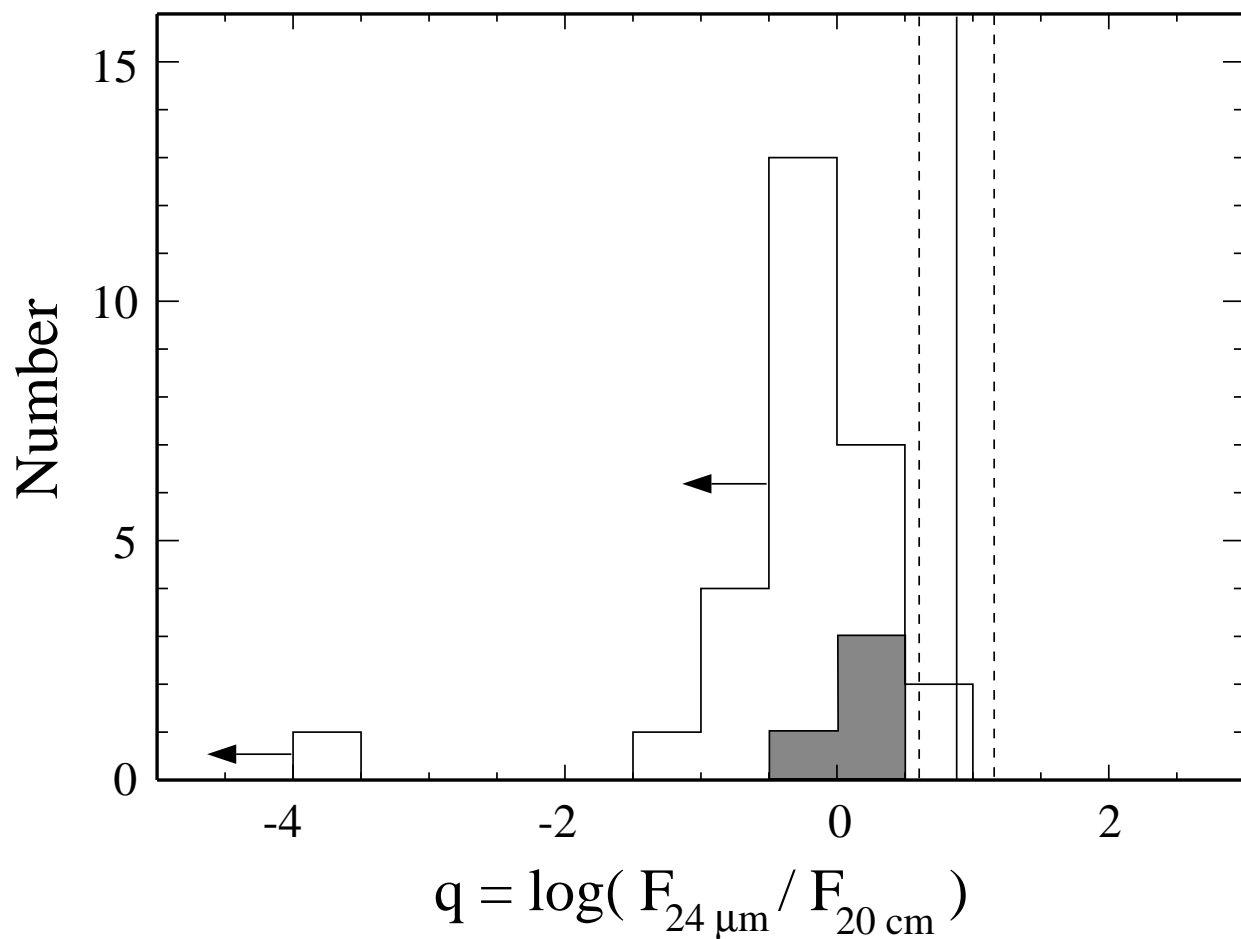


Fig. 4.— Distribution of q for the OIRS sample. The shaded histogram represents the four OIRS detected at $24\ \mu\text{m}$ by MIPS. The unshaded histogram represents upper-limits for q calculated using $F_{24\mu\text{m}} < 0.3\ \text{mJy}$. The vertical solid and dashed lines represent respectively the mean value and range for q in $z \lesssim 2$ starburst dominated systems as determined by Appleton et al. (2004).

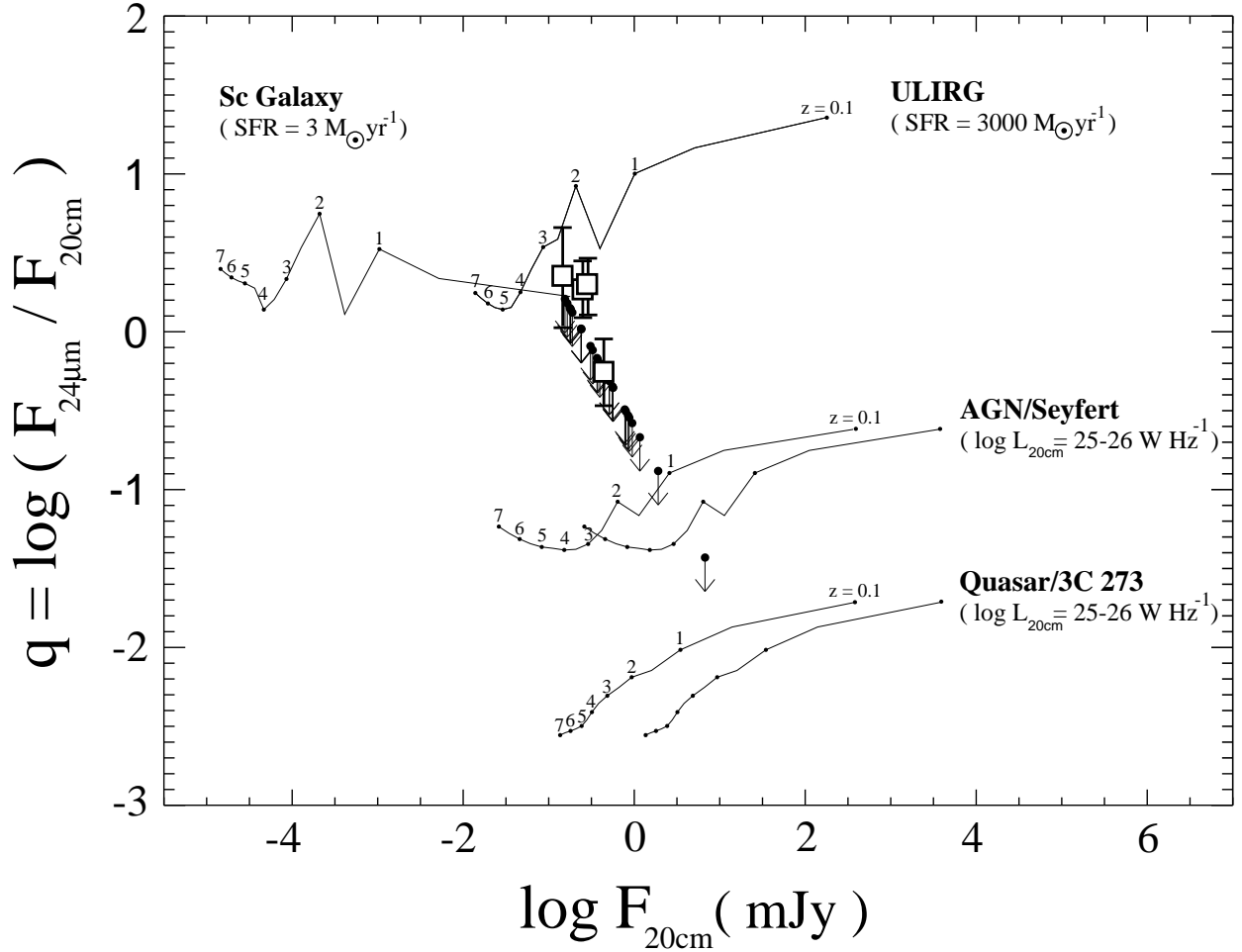


Fig. 5.— Infrared/Radio color-magnitude diagram. The four sets of tracks show the expected infrared to radio flux density ratio versus radio flux density for various SEDs as a function of redshift. Top to bottom: a $\text{SFR} = 3 M_{\odot} \text{ yr}^{-1}$ late spiral, a $\text{SFR} = 3000 M_{\odot} \text{ yr}^{-1}$ ULIRG, a Seyfert AGN with 20 cm luminosities of 10^{25} and $10^{26} \text{ W Hz}^{-1}$, and a quasar with 3C 273’s SED and 20 cm luminosities identical to the Seyfert galaxy’s. Redshift is indicated along the tracks. The large unfilled squares represent the four OIRSs detected at $24 \mu\text{m}$. The small filled circles with arrows are upper-limits for the remaining 27 OIRS not detected by MIPS.

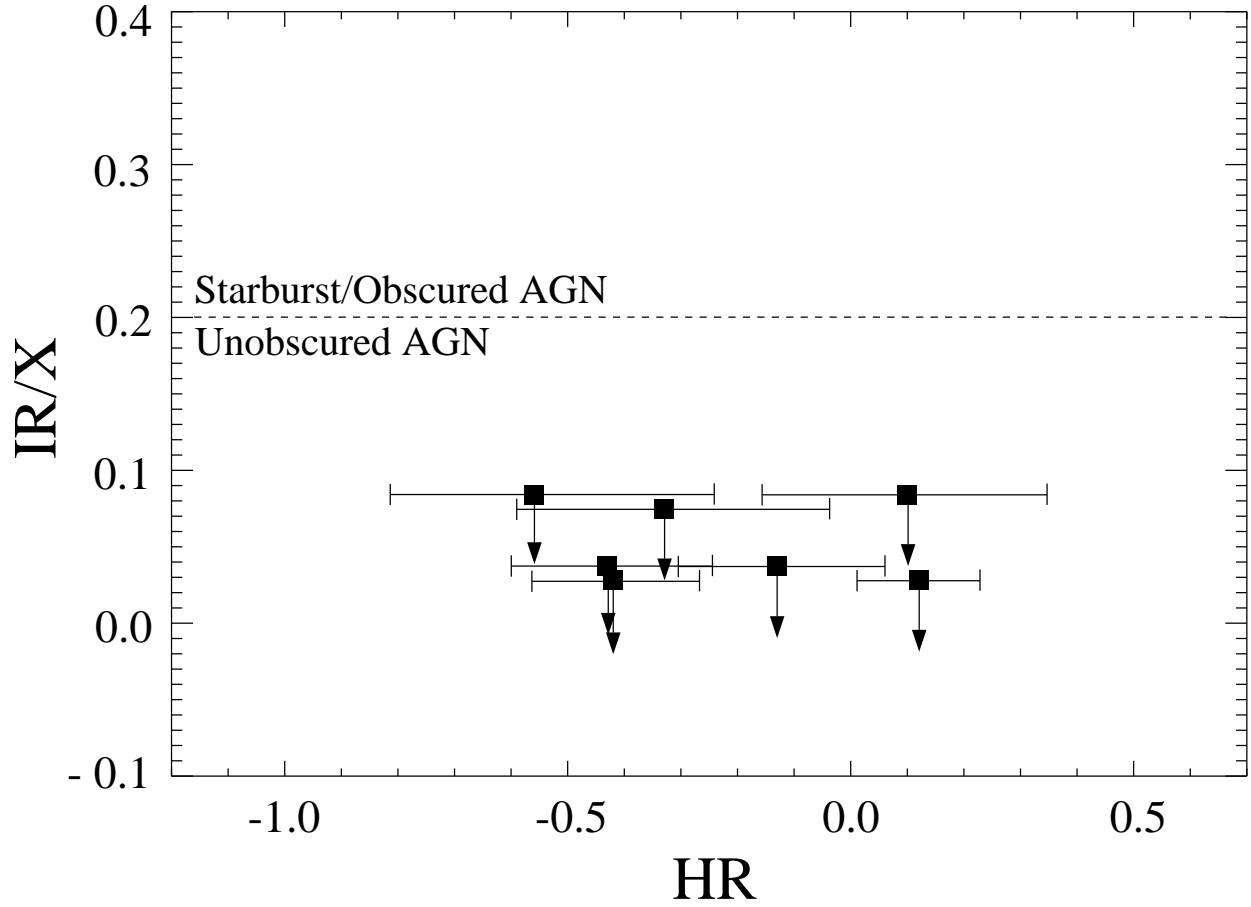


Fig. 6.— The infrared to X-ray ratio (IR/X) versus the X-ray Hardness ratio (HR) for the seven optically invisible X-ray sources detected in the Chandra “soft” 0.5-2 keV band. The dashed line marks $IR/X = 0.2$, which separates starburst and obscured AGN powered emission ($IR/X > 0.2$) from systems dominated by unobscured AGN ($IR/X < 0.2$).

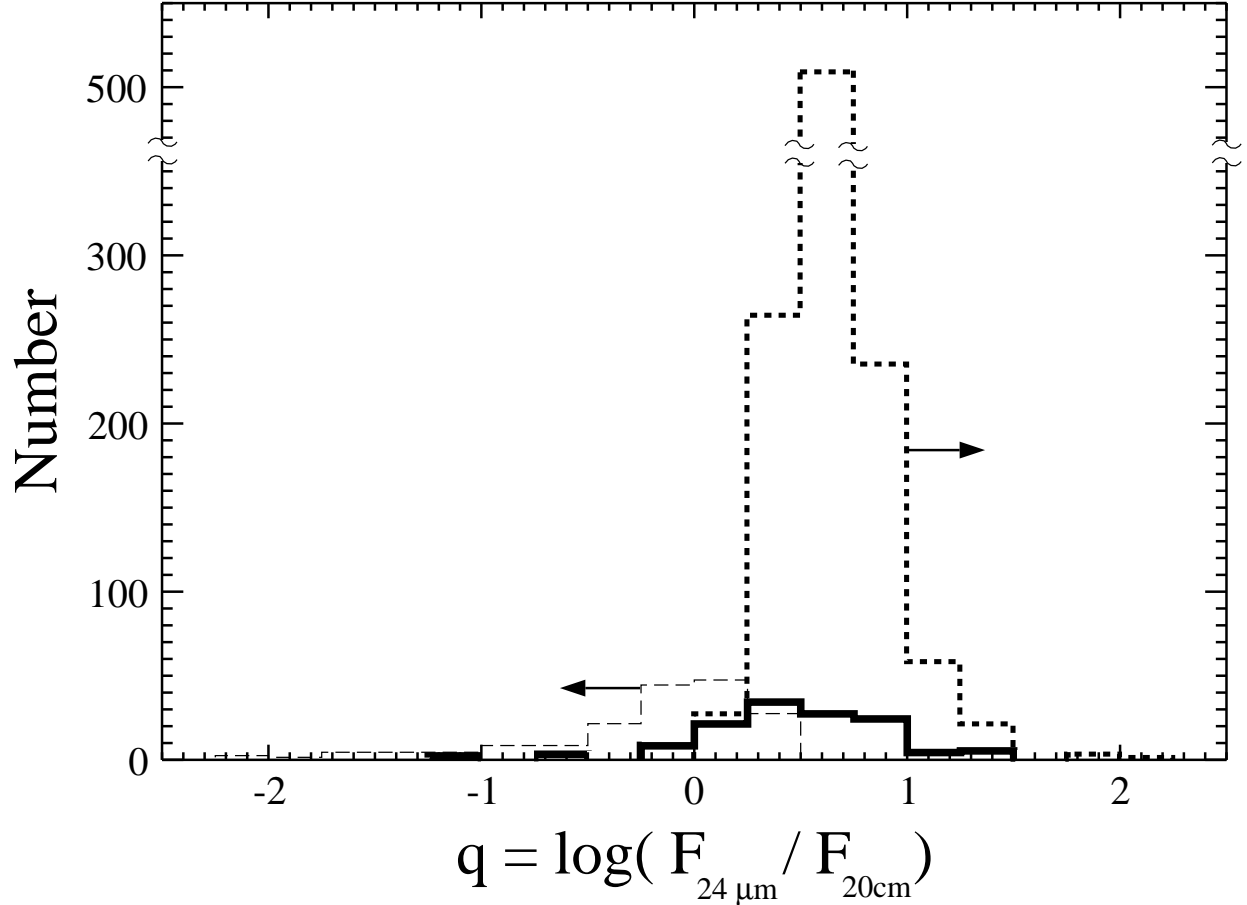


Fig. 7.— Distribution of q for the full radio and infrared sample. The thick solid-line histogram depicts q for the 125 sources detected at both $24 \mu\text{m}$ and 20 cm . The thick-dashed line histogram shows q lower-limits for the 1086 sources detected only in the infrared, where the $F_{20\text{cm}}$ upper-limit was taken to be a point source with $5\times$ the rms at the sources position in the final radio image. All sources in the histogram lie within or to the right of the bins shown. The thin-dashed line histogram shows the 194 radio source’s not detected by MIPS, assuming a $24 \mu\text{m}$ flux upper-limit of 0.3 mJy . Similarly, the sources in this histogram will lie within or to the left of the bins indicated.

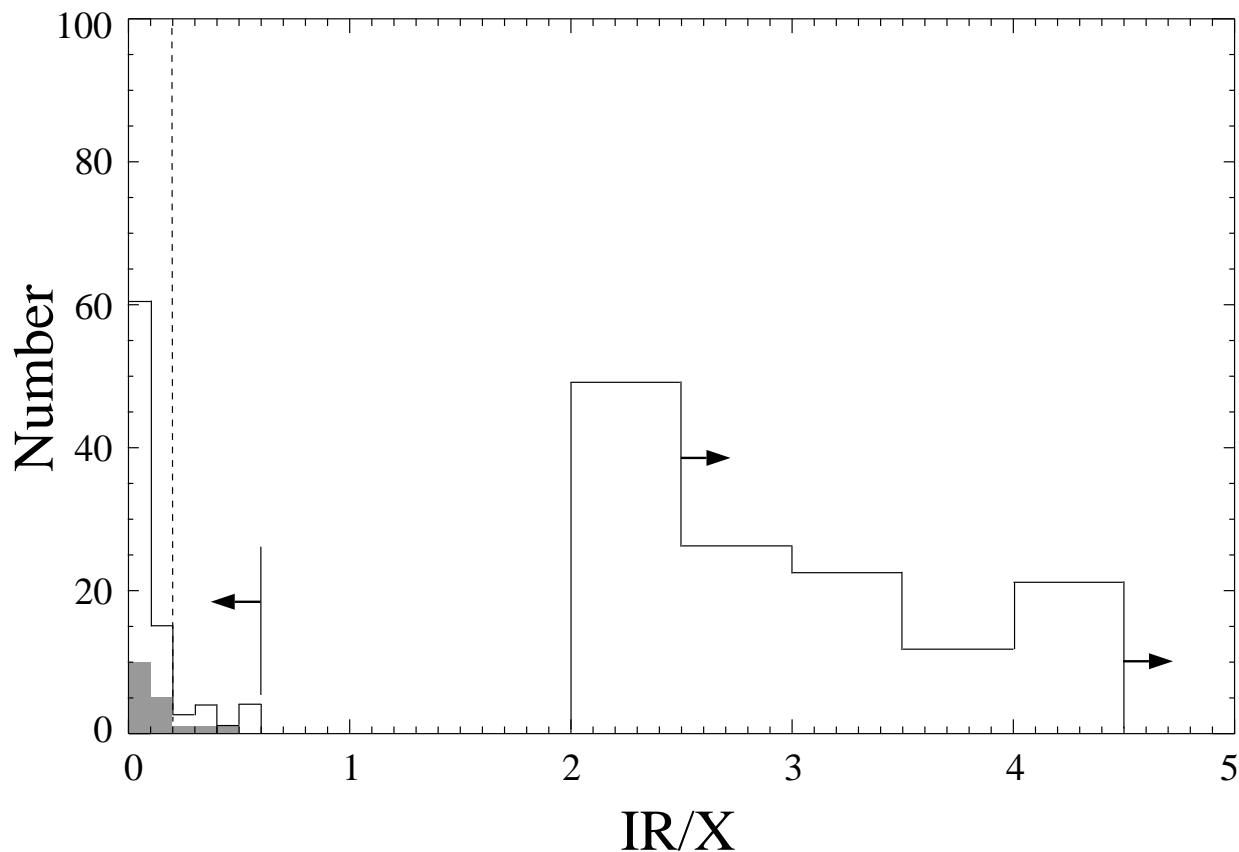


Fig. 8.— The distribution of IR/X for the full sample of infrared and X-ray sources in the overlapping survey area. The shaded histogram shows values of IR/X for the 18 objects detected in both MIPS 24 μm and Chandra 0.5-2 keV band emission. The unshaded histograms show upper and lower limits to IR/X for the Chandra-only (left histogram) and MIPS-only (right histogram) detected samples, respectively. Sources with IR/X $>$ 0.2 are consistent with starbursts or heavily obscured AGN, which includes all MIPS-only sources. Sources with IR/X $<$ 0.2 have their luminosity dominated by an relatively unobscured AGN. This encompasses most Chandra-only sources.